Biocompatible copper sulfide–based nanocomposites for artery interventional chemo-photothermal therapy of orthotropic hepatocellular carcinoma

X. Li [a], H.J. Yuan [a], X.M. Tian [a], J. Tang [a], L.F. Liu [b,**], F.Y. Liu [a,*]

[a] Department of Interventional Radiology, The Fifth Medical Center of Chinese PLA General Hospital, Beijing 100039, PR China
[b] Department of Gerontology, Affiliated Hangzhou First People's Hospital, Zhejiang University School of Medicine, Hangzhou, Zhejiang, 310006, PR China

ARTICLE INFO

ABSTRACT

Transcatheter arterial embolization has been considered as a promising targeted delivery approach for hepatocellular carcinoma (HCC). Currently, chemoembolization was the main treatment for unresectable HCC. However, the traditional chemoembolization treatment suffers from undesirable therapeutic effects and serious side-effects. In this study, the doxorubicin (DOX)-encapsulated and near-infrared (NIR)–responsible copper sulfide (CuS)–based nanotherapeutics was developed for magnetic resonance imaging (MRI)–guided chemo-photothermal therapy of HCC tumor in rats. The DOX-loaded CuS nanocomposites (DOX@BSA-CuS) demonstrated distinct NIR-triggered drug release behavior and high photothermal effect. In an orthotopic HCC rat model, DOX@BSA-CuS nanocomposites were selectively delivered to the tumor site *via* the intra-arterial transcatheter. The proposed DOX@BSA-CuS nanocomposites plus NIR laser irradiation exhibited significant tumor growth suppression performance. Moreover, the treatment progress can be monitored by MRI images. Finally, the preliminary toxicity estimate suggested the negligible side-effect of DOX@BSA-CuS nanocomposites during the therapeutic process. These results suggest the clinical translational potential possibility for imaging-guided arterial embolization with DOX@BSA-CuS nanocomposites for the treatment of HCC.

1. Introduction

Hepatocellular carcinoma (HCC) is one of the most common malignant cancers with high morbidity and mortality worldwide [1,2]. Currently, surgical resection remains the preferred treatment of HCC, but merely less than 20% of patients are candidates because of the late definitive diagnosis and the lack of the available donors [3–5]. In all non-surgical treatment algorithms for HCC, transcatheter arterial chemoembolization (TACE) combined with transarterial infusion (TAI) and transarterial embolization would increase the concentration of chemotherapeutic agents at the tumor region to kill tumor cells, efficiently. Meanwhile, the vessels supplying blood to the tumor region could be embolized to block tumor blood supply, leading to ischemia, hypoxia, and necrosis [6–9]. Therefore, TACE is currently an important therapeutic method that has been widely applied for local treatment of HCC, clinically.

However, there still exist some restrictions of conventional TACE by

transcatheter intra-arterial delivery to HCC tumor [6–9]. The treatment efficacy and safety of traditional TACE approaches may be the main concern because of the uncontrolled drug release behavior, sole functionality, and serious adverse effects [10–12]. Given this situation, previous studies have proved that drug-eluting beads (DEBs)–TACE possessed controlled drug-release characteristics [13]. However, there are still some inevitable functional drawbacks (e.g. lacking of multimodal therapy strategies) for current DEBs-TACE [14]. Therefore, TACE agents combined with other kinds of therapeutic capabilities would solve the limitations of TACE and may be the alternative to provide greater treatment efficacy.

Nano/micro material–based therapeutics have been widely used for embolic and drug-delivery systems *via* TAI injection, exhibiting high tumor cell uptake efficiency and less side-effect to surrounding normal tissues [15–17]. Recently, nanomaterials with photothermal conversion performance by near-infrared (NIR) irradiation have been widely utilized for photothermal therapy (PTT) of tumors [18–21]. These nanoparticles

(NPs) are always multifunctional with simultaneous diagnosis and therapy performance. Meanwhile, the controlled drug delivery behavior could also be obtained. Semiconductor CuS NPs are http://dict.youdao.com/w/frequently-used photothermal agents because of the broad absorption in the NIR region from 700 to 1100 nm and can generate heat for PTT of cancer cells [22]. Moreover, CuS NPs possess less toxicity, low cost, facile synthesis, and high photothermal conversion efficiency, which have been developed for cancer imaging and therapy [23–26]. Meanwhile, the CuS NPs can only induce toxic effects at relative high concentrations. The expression of oxidative stress–related genes is not impacted by the presence of the CuS-based NPs [27]. Therefore, CuS NPs could be an excellent candidate for the photothermal component in embolic agents.

Nano-therapeutics could be delivered to the tumor region following systemic administration *via* enhanced permeation and retention effect [28–30]. However, the tumor-specific uptake efficiency is relatively low, and most of the injective doses are intercepted by the reticuloendothelial system [31]. Inevitably, a massive off-target dose may cause unsatisfactory therapeutic effect and long-term toxicity concerns. In this study, a minimally invasive interventional clinical technique was applied to directly delivery the therapeutic agents into the tumor site through the arterial blood vessels at tumor tissue. CuS NPs served as a photothermal agent. With the surface modification with bovine serum albumin (BSA) molecules, as a biocompatible template for the synthesis of NPs, an antifouling molecule and a viable drug carrier for chemotherapeutic drugs, which could stabilize nanostructures, reduce the adhesion of blood cells to improve the capture purity of HCC [22,32]. Doxorubicin (DOX) loading and NIR-responsible release behavior were carefully investigated. Lipiodol, utilized as an embolic, fixed the DOX@BSA-CuS deposition around liver tumor and promoted the entry efficiency of NPs into tumor tissue. Hepatic artery injection of DOX@BSA-CuS mixed with Lipiodol can improve the photothermal-chemoembolization therapy of HCC in the rat model (Scheme 1). In our study, the preparation process of DOX@BSA-CuS NPs is not complex, no toxic substances are utilized during the preparation process, and it guarantees high biosafety. Moreover, the DOX@BSA-CuS NP products possess good stability. Finally, the drug concentration in the HCC tumor region can be increased by local administration, which is in favor of more efficient and safe treatment.

2. Material and methods

2.1. Synthesis of BSA-modified copper sulfide NPs (CuS-BSA NPs)

The CuS NPs were synthesized by following previously reported studies [33]. The typical synthesized method was as follows. A total of 250 mg of BSA powder and 120 mg of copper nitrate Tri hydrate were separately dissolved in 50 mL of deionized water, and the mixture was stirred at room temperature (1200 rpm/min) until it forms a light blue solution. A nitric acid solution was further added slowly under stirred condition to adjust pH to 3.0. Subsequently, 0.2 M of thioacetamide solution was added, and the color of the solution turned to yellow gradually. The mixture was heated at 90 °C until the color of the solution turned to dark green. Finally, BSA-CuS NPs were collected after centrifugation at 13,000 rpm/min for 30 min and washed with deionized water. BSA-CuS NP powder samples were obtained by the freeze-drying method.

2.2. DOX loading and release behavior

A 50 mg of BSA-CuS NP powder was added into 20 mL of DOX aqueous solution (1 mg/mL) and stirred overnight. Subsequently, the free DOX was removed by centrifugation to obtain the DOX-loaded BSA-CuS (DOX@BSA-CuS) NPs. The total loaded DOX drugs were examined by using an ultraviolet–visible (UV–vis) spectrophotometer (UV-2600, Shimadzu Co., Ltd.) at a wavelength of ~480 nm. Specifically, the

loading rate was calculated by subtracting the original and remaining DOX content. The NIR-triggered DOX release behavior was further studied by soaking 50 mg of DOX@BSA-CuS NP samples in 20 mL of phosphate-buffered saline (PBS) with the pH = 7.4. At different time intervals, 5 mL of solution was obtained and replaced with equal volume of fresh PBS. The content of released DOX molecules under NIR or without NIR irradiation was calculated by using the UV–vis spectrophotometer. The total released DOX content was counted based on the following formula: release percentage = (cumulative amount of DOX released at each time point)/(amount of total DOX loaded on the BSA-CuS) *100%.

2.3. In vitro cell studies

The N1–S1 HCC cells (ATCC, Manassas, VA, USA) were evenly suspended in a 75 cm^2 culture dish containing 10% fetal calf serum (Gibco) and 1% IMDM culture medium with penicillin-streptomycin (Iscove's Modified Eagle Medium, Gibco) and placed in an incubation chamber (Thermo Scientific, USA) containing 5% CO_2 at 37 °C. The N1–S1 cells were incubated with DOX and DOX@BSA-CuS for 2 h and were exposed to 1.5 W/cm^2 808 nm laser irradiation for 5 min. Subsequently, the cells were incubated for another 2 h, and the photothermal influence on cellular viability was further explored.

An Annexin V-FITC Apoptosis Detection Kit 2.3 (Sigma) was utilized to study the N1–S1 cell apoptosis under different treatments. The following processes were used: (1) Preparation of cells: the N1–S1 cells were incubated overnight in a 24-well plate. (2) Therapeutics induction: the collected cells were suspended in the drugs (free DOX, DOX@BSA-CuS NPs, and pure culture medium), diluted with 500 μL serum-free IMDM, and placed in triplicates. The cells were then incubated in a dark incubation chamber at 37 °C for 4 h and re-suspended in serum-free IMDM, and NIR laser irradiation was performed using the foregoing induction parameters. (3) Cell treatment: under NIR irradiation, the suspension was rinsed twice with PBS and centrifuged (2000 rpm, 5 min) to collect the cells. (4) Addition of samples: after using 500 μL of Binding Buffer to suspend the cells, 5 μL of Annexin V-FITC was added, and 5 μL of propidium iodide was added after stirring thoroughly. The suspension was allowed to react at room temperature for 5–15 min and then placed in a flow cytometer (FC500, Beckman Coulter Ltd.) to measure cell necrosis. Annexin V-FITC was measured *via* the FITC channel (FL1), and propidium iodide (PI) was measured via the FL3 channel.

2.4. Intrahepatic arterial cannulation procedures

The experiments were performed on the 8th day when the volume of tumor increased to 29.85 ± 10.11 mm^3. The procedure of transcatheter arterial injection of therapeutic agents was shown in Fig. 5. The gastroduodenal artery was freed with vascular forceps, and two 4.0 F sutures were set at the proximal and distal ends. After the ligation of the distal end, a 24G indwelling needle (Braun, Malaysia) was inserted into the gastroduodenal artery. Guided by a 2.2F guide wire (Japan Asahi INTECC, STD 130-22S), the indwelling needle was pushed into the hepatic artery under direct vision, and the proximal end was lightly tightened to fix the indwelling needle and prevent it from becoming loose. Different treatments were administrated into the hepatic artery. The treated methods were specified as the following groups, the control, DOX+Lipiodol, BSA-CuS+Lipiodol+NIR, DOX@BSA-CuS+Lipiodol, and DOX@BSA-CuS+Lipiodol+NIR, and 5 rats were present in each group. After completion of the drug administration, the indwelling needles were removed, while the near-end was sutured to stop bleeding. The incisions were sutured in layers when no bleeding was ensured. The intramuscular injection with penicillin lasted for three days. After the different treatments for 6 h, the photothermal treatment groups were separately irradiated with 808 nm NIR irradiation at a power density of 1.5 W/cm^2 for 5 min.

2.5. Magnetic resonance imaging

To monitor the therapeutic effect properties after different treatments, a 1.5 T superconducting magnetic resonance imaging (MRI) machine (Optima 360 Advanced, GE) was used to perform T_2 fast recovery fast spin echo (T_2 FRFSE) sequence observations preoperatively and 3, 7, and 10 d postoperatively, with the following scanning parameters: flex small coil, repetition time (TR) (4500–5000) ms, echo time (TE): 102 ms, array: 256 × 256, FOV 8–10 cm, slice thickness: 3.0 mm, and slice interval: 0 mm. Measuring the tumor's largest diameter and transverse diameter was set as A and B, respectively, and the tumor volume (V) was calculated based on $V=(A \times B^2)/2$.

2.6. Detection of DOX release in vivo

After injection with the DOX@BSA-CuS nanocomposites by the hepatic artery, rats were sacrificed at different time points of 1, 6, and 24 h. Tumor tissues were collected and sliced into 5 mm using a cryostat (Germany, FRICELL CM1950). The released DOX fluorescence at the tumor site was observed with a fluorescence microscope (Japan, OLYMPUS IX73) under an emission wavelength of ~480 nm.

2.7. Histology and immunohistochemistry and biosafety evaluation

To investigate the therapeutic efficacy after different treatments, the rats in all groups were sacrificed at 10 days postoperatively, and 10% formalin was used to fix the liver tumor specimens. The specimens were coated with paraffin after 24 h, and slices with a thickness of 5 μm were prepared. After dewaxing and hydration, the slices were subjected to Hematoxylin-eosin (H&E), TUNEL, Ki67, CD31, and Caspase 3 staining, which allowed the tumor tissue's general characteristics and tumor cell necrosis, proliferation, microvessel density, and synergistic phototherapy to be observed. All slides were analyzed with a TissueFAXS microscope (Tissue Gnostics GmbH, Vienna, Austria). IOD, defined as the integrated optical density, is a generally utilized method for quantitative analysis of immunohistochemical data.

The tail arterial blood of Sprague Dawley (SD) rats was collected before and after different treatments for 1, 3, 7, and 10 days. A Cobas 8000 instrument (Roche, Germany) was used to determine the levels of alanine transaminase (ALT), aspartate transaminase (AST), creatinine (CREA), and blood urea nitrogen (BUN) to assess the hepatorenal and renal function–related toxicity.

3. Results and discussion

3.1. The characteristics of BSA-CuS NPs

The preparation process of BSA-CuS NPs and the utilization as a therapeutic agent for chemo-photothermal systematic treatment of N1–S1 HCC cells and orthotopic liver tumor are illustrated in Scheme 1. As illustrated in Fig. 1a, the transmission electron microscopy (TEM) image showed the morphology of the CuS NPs and the diameter size distributed in the range of 40–60 nm. In addition, the inset selected area electron diffraction (SAED) pattern indicated distinct diffraction rings, meaning the crystalline structure. The lattice fringes are distinct in the high resolution transmission electron microscopy (HRTEM) image, and the distance of the adjacent lattice fringes is ~0.281 nm, consistent with the lattice plane spacing of (103) of the covellite hexagon of CuS crystal structure (Fig. 1b). The X-ray diffraction pattern of CuS NPs belongs to the covellite hexagonal phase (JCPDS No. 65-603) [34]. The emerging peaks at (101), (102), (103), (110), (108), and (116) planes demonstrate the pure crystalline feature of CuS NPs (Fig. 1c). Furthermore, the UV–vis spectrum of CuS NPs demonstrates a wide absorption peak in the NIR region (Fig. S1). CuS nanomaterials, as typical photothermal agents, have been widely studied in biomedical application [35,36]. Consequently, the photothermal performance of the CuS NPs was carefully investigated
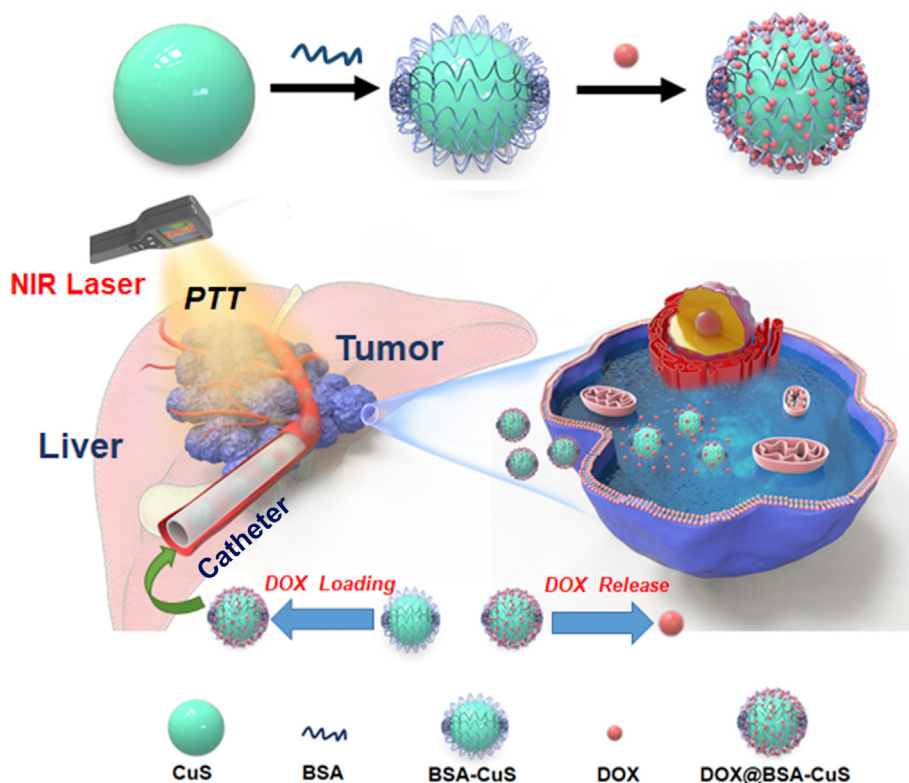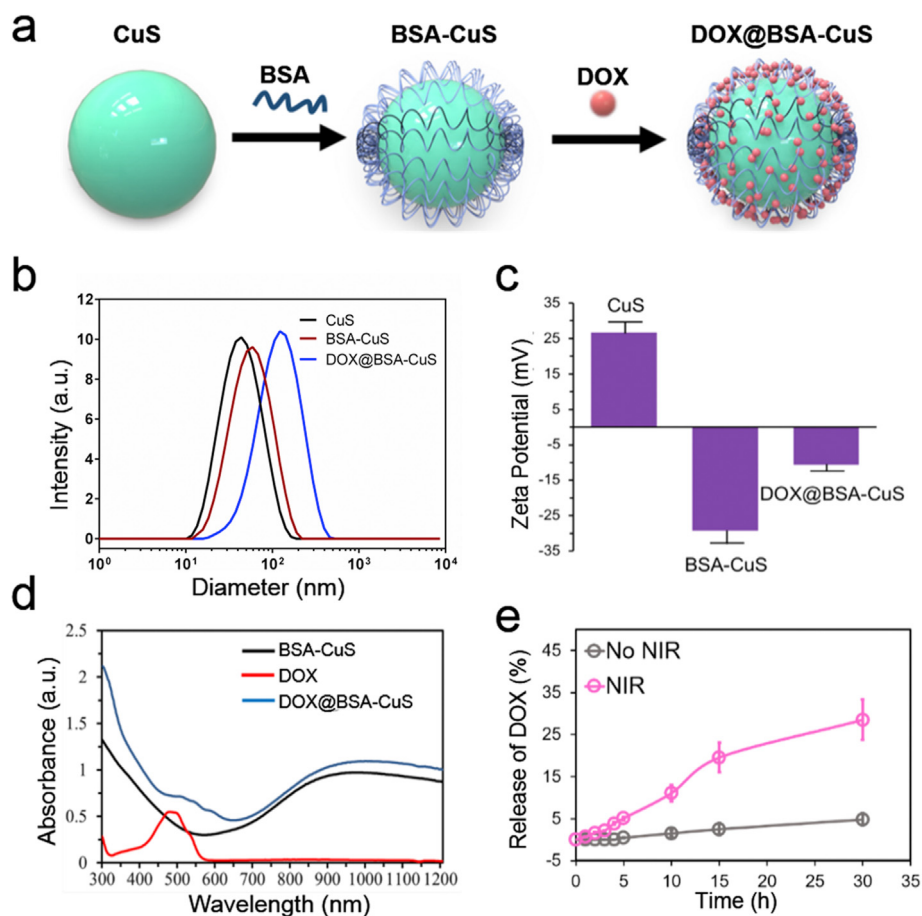

Scheme 1. Schematic illustration of DOX@BSA-CuS NP preparation and synergistic therapy of orthotopic liver cancer by chemo-photothermal treatment through an intra-arterial intervention administration process.
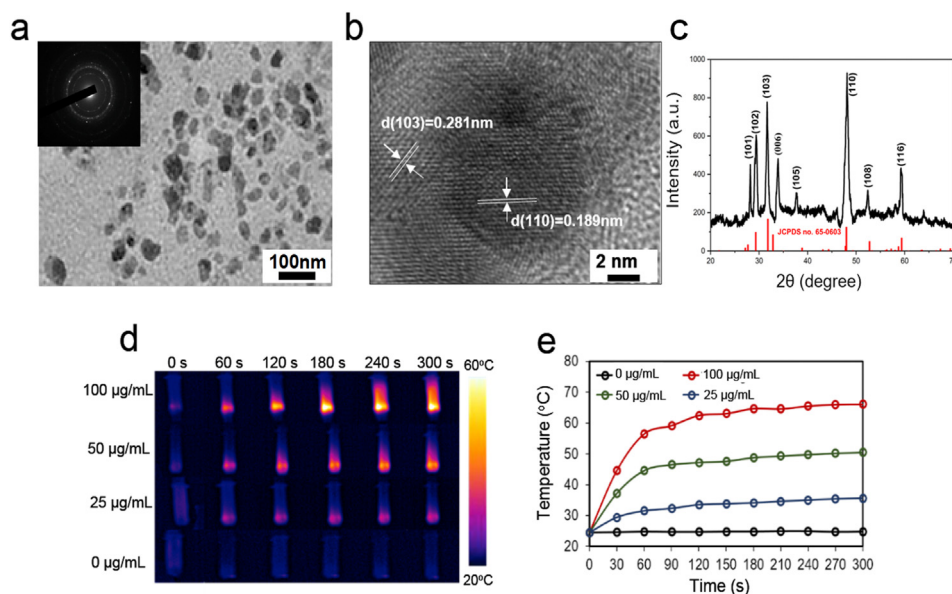
Fig. 1. Characterization of CuS NPs. (a) The TEM image of CuS NPs (the inset shows the corresponding SAED pattern). (b) The HRTEM image of CuS NPs. (c) X-ray diffraction patterns of crystalline CuS NPs. (d) Thermal images of BSA-CuS aqueous solution with different concentration after exposed to the NIR laser (808 nm) at 1.5 W/cm². (e) Temperature changes of BSA-CuS at different concentrations after irradiated with an NIR laser at 1.5 W/cm².

via recording the changes of the temperature under NIR (808 nm) laser irradiation. As revealed in Fig. 1d and e, the temperatures of all the CuS NP solution increased along with the prolonged irradiation time.

Meanwhile, the temperature rises faster as the concentration of CuS NPs increased. After exposed to NIR irradiation for 300 s, the temperature of CuS NP solution can reach ~62 °C with the concentration of 1.0 mg/mL.

Fig. 2. Characterization of DOX@ BSA-CuS. (a) Schematic illustration of the modification and DOX loading process. (b) Hydro diameters of CuS NPs before and after the BSA modification process. (c) The corresponding zeta potential changes after BSA modification and subsequent DOX loading. (d) UV–vis spectra of BSA-CuS, DOX molecule, and DOX@BSA-CuS. (e) Cumulative DOX molecule release profiles of DOX-loaded BSA-CuS with or without NIR irradiation.

However, the recorded temperature of pure water solution remains nearly constant. Meanwhile, the photothermal conversion efficiency (η) was carefully calculated as per the previous method [37], and the value is ~ 46.28% (Fig. S2). These results suggested effective photothermal performance of the CuS NPs under 808 nm NIR irradiation.

3.2. NIR-responsible drug release and in vitro anticancer efficacy

The DOX@ BSA-CuS was prepared based on the schematic illustration in Fig. 2a. The mean hydrodynamic diameter of CuS NPs was determined to be ~70 nm by dynamic light scattering (DLS) and represented narrow size distribution (Fig. 2b). The sizes measured by DLS were mildly increased with the surface BSA modification (~90 nm). After loading the DOX, the final hydrodynamic diameter of the NPs is ~99 nm. Moreover, the DOX@BSA-CuS can be well dispersed in pure water, Phosphate buffered saline (PBS), Fatal bovine serun (FBS), Dulbecco's modified Eagle's medium (DMEM), and DMEM + 10% FBS solution. The hydrodynamic diameters of DOX@BSA-CuS were mildly changed after dispersed in different solution for 7 days and demonstrated well stability (Fig S3). Meanwhile, the morphology of the BSA-CuS NPs was

characterized by TEM, and they almost retain the morphology and crystal structure feature with respect to CuS NPs (Fig. S4). Meanwhile, the zeta potential of CuS NPs varied from 26.5 to −30.3 mV because of the BSA molecule modification (Fig. 2c). It has been reported that DOX could be effectively loaded onto the surface of BSA@CuS, forming BSA@-CuS@DOX NPs through electrostatic interactions between negatively charged BSA@CuS and positively charged DOX [38]. The loading rate was calculated by subtracting the original and remaining DOX content based on the standard curve of the DOX drug (Fig. S5). The capsulation rate and loading rate of DOX were 55.52%. In this study, the DOX drug, with positive zeta potential of 2.2 mV, intends to link to BSA-CuS NPs with negative zeta potential (−30.3 mV) through the electrostatic interaction. One notes the fact that the changes of zeta potential demonstrated the successful BSA molecule modification and DOX drug loading process (Fig. 2c). The UV–vis spectrum of DOX solution exhibited a characteristic peak at ~480 nm. After the DOX loading process, the DOX@BSA-CuS exhibited the overlapping peak of the DOX molecule, implying the successful DOX loading (Fig. 2d). Subsequently, the drug release behavior of DOX@BSA-CuS in a neutral PBS solution (pH = 7.4) with or without NIR irradiation was studied. As shown in Fig. 2e, ~1.5%
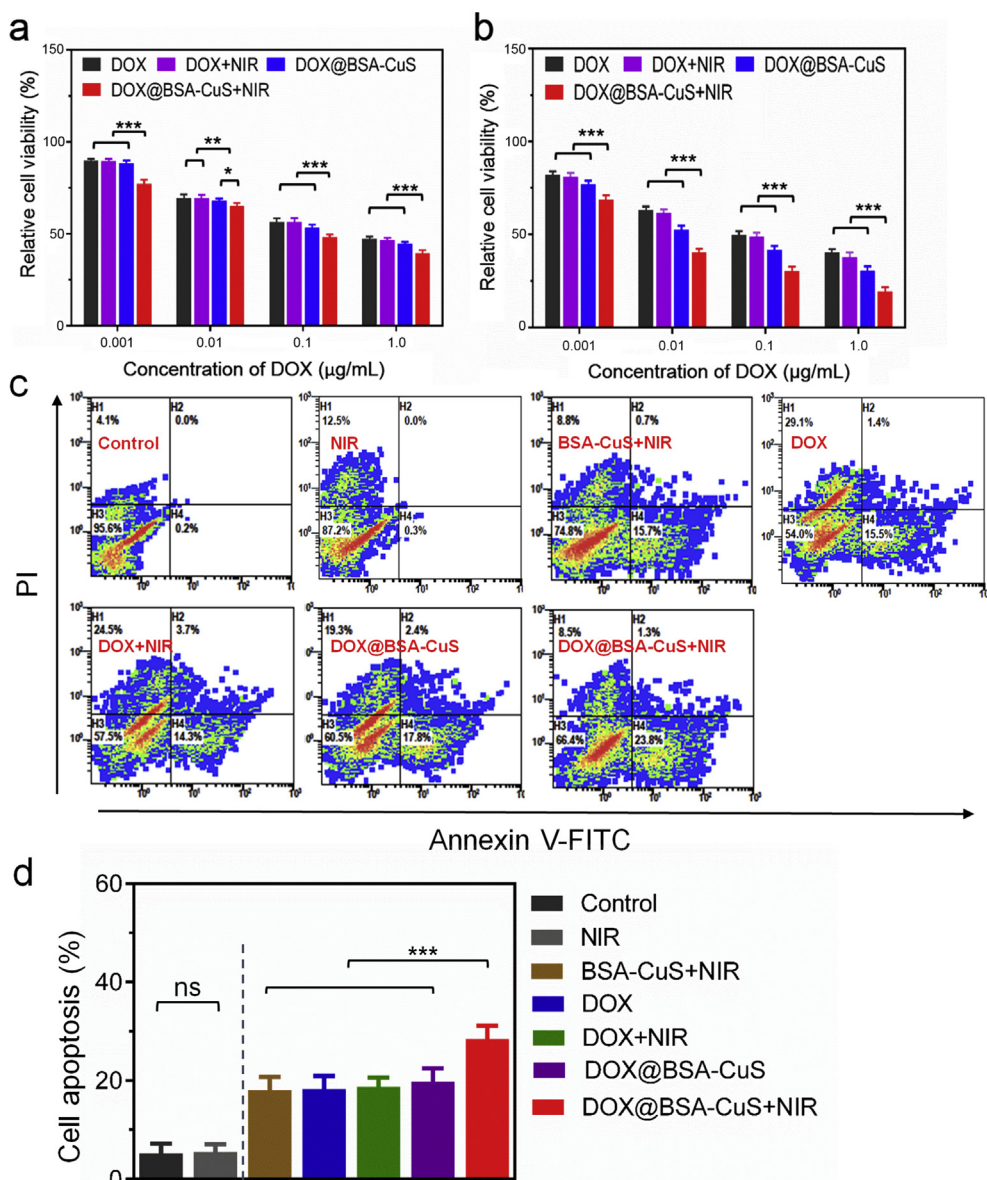

Fig. 3. In vitro N1–S1 cancer cell viability and synergistic phototherapy of DOX@ BSA-CuS. (a) and (b) Relative N1–S1 cancer cell viability (to blank control) of free DOX, DOX+NIR, DOX@BSA-CuS, and DOX@BSA-CuS+NIR (1.5 W/cm^2, 5 min) at 24 h and 48 h, respectively. (c) Evaluation of apoptosis rates of N1–S1 cells by flow cytometry analysis with different treatments at 24 h. (d) The corresponding quantitative apoptotic measurement of N1–S1 cells at 24 h. Note: *P < 0.05, **P < 0.01, ***P < 0.001, and ns represents no significance.
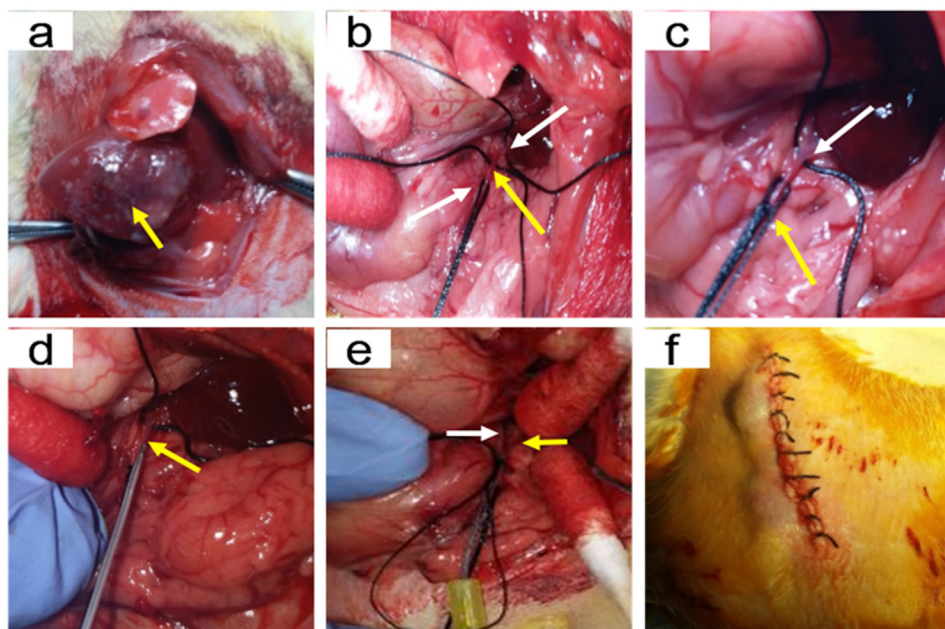
Fig. 4. Intra-arterial administration of therapeutic agents by the hepatic artery in rats bearing N1–S1 HCC tumor. (a) Liver tumor (yellow arrow). (b) The gastroduodenal artery (yellow arrow) was identified and freed at the near and far ends by two 3.0 F sutures (white arrow). (c) The distal gastroduodenal artery (yellow arrow) was ligated with sutures. (d, e) The gastroduodenal artery was punctured by a 24G indwelling needle (yellow arrow), and a cannula was placed into the hepatic artery (white arrow). (f) After the administration of the therapeutic agents, the cannula was removed, the proximal gastroduodenal artery was tied off, and the operative site was stitched up.
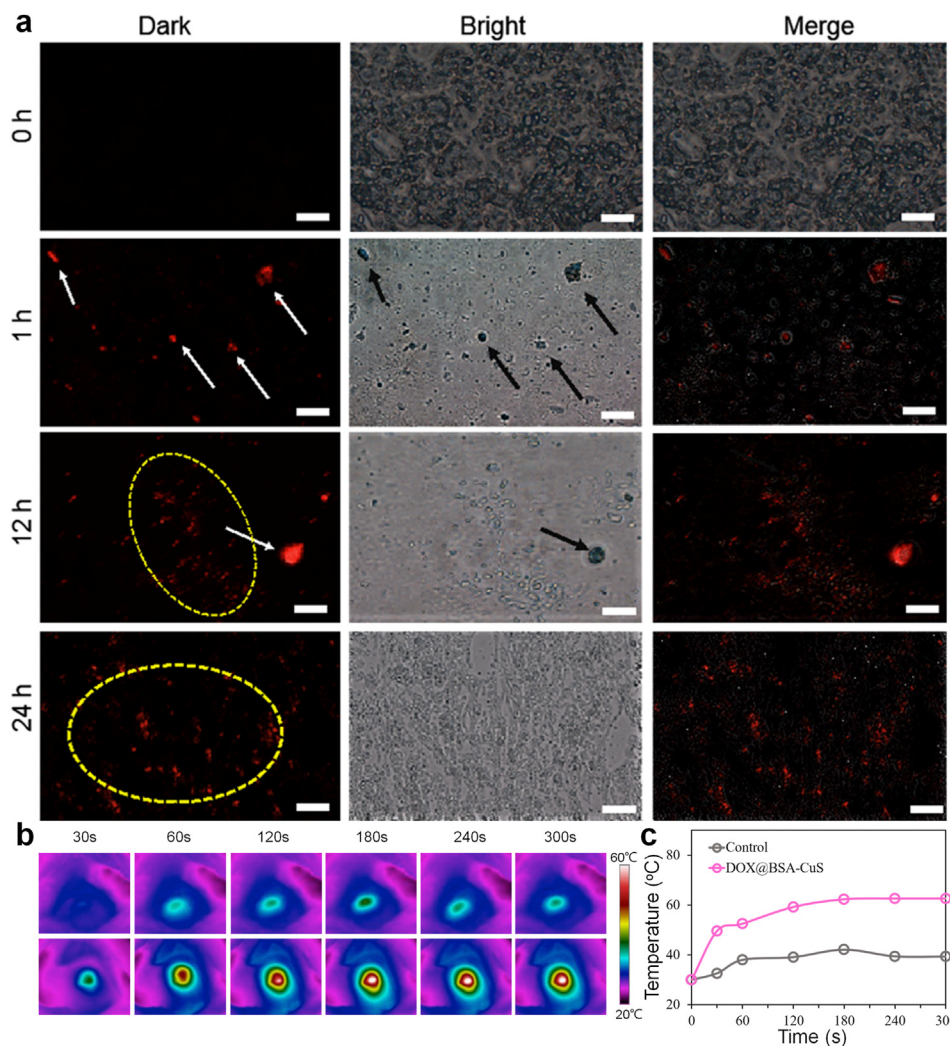
Fig. 5. *In vivo* investigation of DOX delivery and photothermal performance of DOX@BSA-CuS. (a) *In vivo* immunofluorescence staining of DOX molecules (red fluorescence). Fluorescence images of slices harvested from the tumor section after intra-arterial injection of DOX@BSA-CuS. (b) Thermal images of the tumor section under NIR laser irradiation with power density of 1.5 W/cm^2 after intrahepatic arterial injection procedure with 0.4 mL BSA-CuS NPs (the concentration is 1 mg/mL). (c) *In vivo* tumor region temperature change curves after irradiated with NIR laser irradiation for 5 min. Note: scale bar = 200 μm.
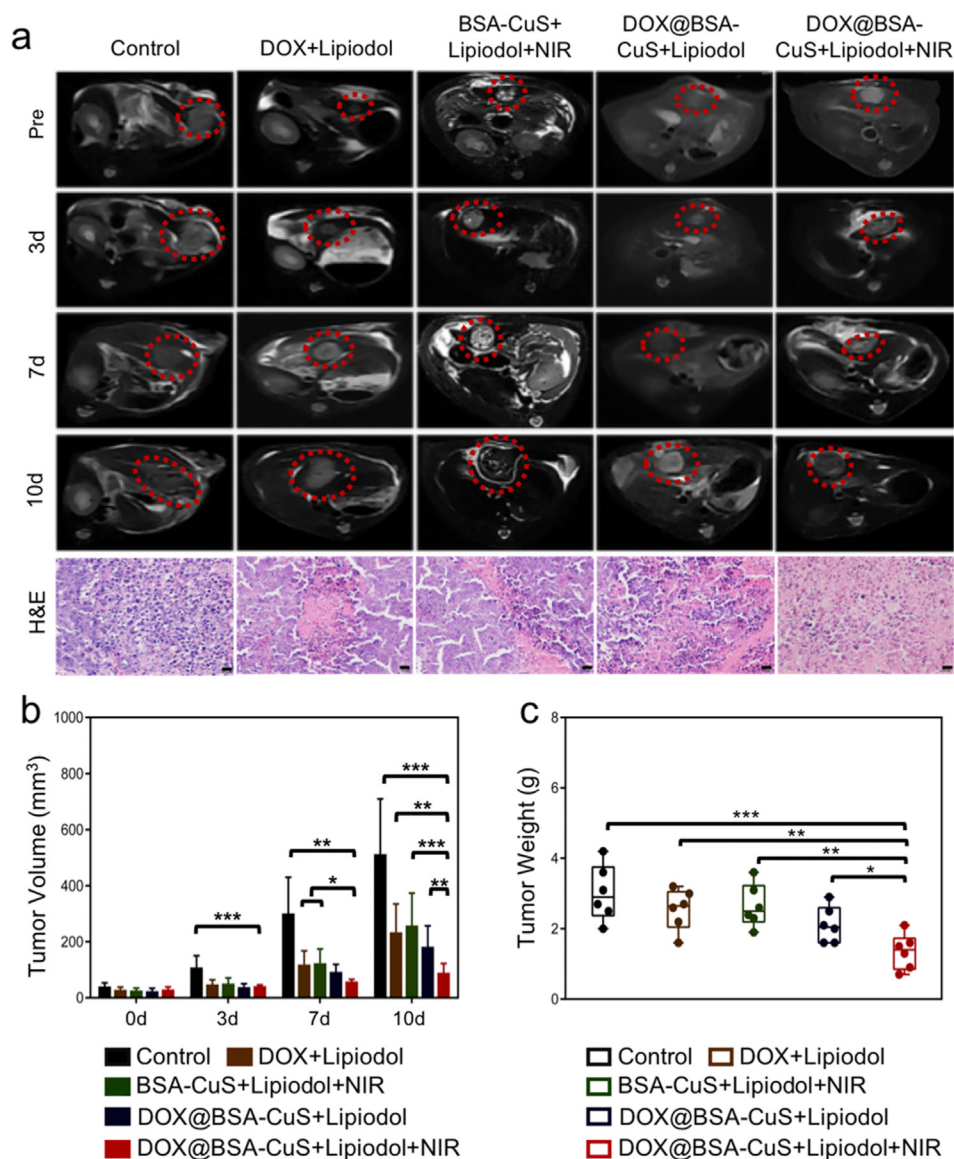
Fig. 6. *In vivo* MRI-guided therapeutic efficacy using the orthotopic N1–S1 HCC tumors in the SD rats. (a) MRI imaging was performed at 0, 3, 7, and 10 days after transcatheter infusion to detect the tumor volume variation (the red circle represented the tumor section) and representative H&E staining of tumor tissue sections at 10 days after different treatments. The scale bar is 20 μm. (b) Changes of HCC tumor volume as a function of time after different treatments. (c) Tumor weights of dissected tumors at 10 days after treatment. (n = 5, *P < 0.05, **P < 0.01, ***P < 0.001).

of DOX was liberated at the time point of 10 h, and ~5% of the accumulative DOX was liberated within 30 h. On contrast, relatively fast drug release kinetics was observed after exposed to 808 nm NIR irradiation. ~5% and ~25% of total DOX were released at 5 and 24 h, respectively. The results demonstrated that the NIR light exposure has promoted the DOX molecule release rate from DOX@BSA-CuS. Such stimulus release under NIR irradiation can be attributed to the heating effect of BSA-CuS NPs, which reduced the electrostatic bond between DOX and BSA-CuS NPs [39]. Finally, the 3-(4,5-Dimethylthiazol-2-yl)-2,5-diphenyltetrazolium bromide (MTT) assay was conducted to investigate the cytotoxicity of BSA-CuS. As demonstrated in Fig. S6, the relative cell viability was over 80% within the concentration of 100 μg/mL with the increased concentration after incubation for 24 and 48 h. Above mentioned results reflect that the BSA-CuS possess low cell cytotoxicity under a concentration range, which is consistent with the other reports.

To assess *in vitro* cancer cell–killing ability of the DOX@BSA-CuS under NIR irradiation, N1–S1 cancer cells were cultured with different doses of DOX or DOX@BSA-CuS solution with or without NIR irradiation. As shown in Fig. 3a and b, the relative viability of N1–S1 cancer cells cultured with DOX@BSA-CuS was decreased gradually at the DOX concentration ranging from 0.001 to 1.0 μg/mL. After exposed to NIR irradiation, the cancer cell–killing ability was enhanced. The relative

viabilities of N1–S1 cells exposed to DOX@BSA-CuS with NIR irradiation at 24 h and 48 h were 39.4% and 19.3% at the DOX concentration of 1 μg/mL, respectively. It is clearly presented that DOX@BSA-CuS can significantly promote the *in vitro* anticancer performance *via* NIR-triggered chemo-photothermal systematic treatment.

Furthermore, flow cytometry was utilized to evaluate the N1–S1 cell necrosis with different treatments (Fig. 3c). N1–S1 cells in the DOX@BSA-CuS group had a higher rate of necrosis (~19.8%) than the control group (~5.2%) and DOX group (~18.3%), which may be due to the enhanced DOX drug delivery efficiency of DOX@BSA-CuS. The N1–S1 cell necrosis in the BSA-CuS+NIR (~18.1%) group exhibited NIR-mediated photothermal effect for cancer cell–killing ability. However, the N1–S1 cell necrosis in NIR and DOX+NIR groups was relatively low, whereas the DOX@BSA-CuS group exhibited significantly increased necrosis after NIR induction. Increased necrosis (~23.0%) in the DOX@BSA-CuS+NIR group was the result of the combined effects of chemo-photothermal systematic treatment.

3.3. Transcatheter intra-arterial process, DOX delivery in tumor, and photothermal property

The process of transcatheter arterial injection of DOX@BSA-CuS was
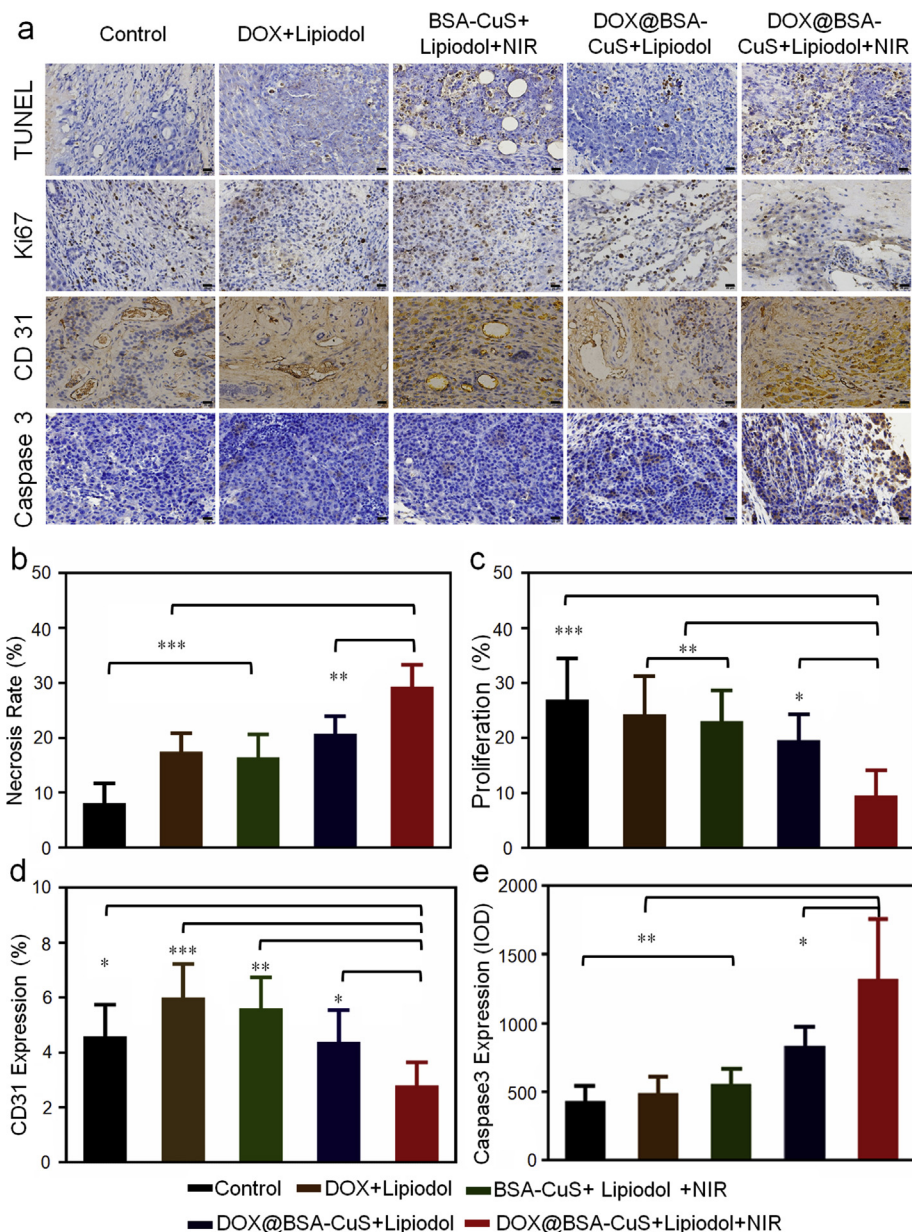
Fig. 7. Immunohistochemical analysis of the tumor tissue at 10 days after treatment. (a) Representative TUNEL, Ki-67, CD31, and Caspase3 staining of tumor tissue sections to assess the efficacy of treatment. (b) The corresponding quantitative analysis of immunohistochemical results. The data were expressed as mean ± SD. Note: the scale bar = 200 μm, *P < 0.05, **P < 0.01, ***P < 0.001.

illustrated in Fig. 4. The distal end of the gastroduodenal artery was ligated with sutures after being freed. The puncture was performed between the proximal and distal ends, and the indwelling needle was set into the hepatic artery. The cannula was removed, the proximal gastroduodenal artery was tied off, and the operative incisions were stitched up after the injection of the DOX@BSA-CuS NPs. TEM was utilized to confirm the internalization of DOX@BSA-CuS in the tumor section after transcatheter arterial administration. The unambiguous TEM images demonstrated DOX@BSA-CuS as dark spots (Fig. S7) in the tumor tissues, indicating the successful transcatheter arterial process. The previous studies have also demonstrated that local drug delivery can be achieved by implanting drug-loaded NPs to the targeted site, which ensured the enhanced dosage at the tumor site and reduced side-effects [40]. In our study, local administration through the hepatic artery ensures that DOX@BSA-CuS can be efficiently delivered to the HCC tumor site. Meanwhile, the combination of Lipiodol not only achieved

chemoembolization for HCC tumor. More importantly, Lipiodol can further improve the uptake efficiency of drug-loaded NPs by HCC tumor [41]. Furthermore, the *in vivo* DOX drug release performance in the tumor site was studied (Fig. 5a). In Fig. 6, there is almost no DOX fluorescence signal that can be detected at a time point of 0 h, implying that the DOX@BSA-CuS NPs have not been injected. However, fluorescence microscopy demonstrated that the DOX@BSA-CuS nanocomposites are mainly distributed in the tumor tissues 1 h after intrahepatic arterial injection. Red DOX fluorescence (white arrow) present within BSA-CuS (black arrow) at the initial 1 h. Subsequently, the DOX was partly released from the DOX@BSA-CuS at 12 h (yellow circle). Subsequently, more DOX drug molecules were released from DOX@BSA-CuS at 24 h and evenly distributed around the tumor region (yellow box). The abovementioned results demonstrated that the DOX@BSA-CuS can be efficiently delivered to the HCC tumor site and the DOX drug can be efficiently deposited at tumor tissue. Therefore, these results have
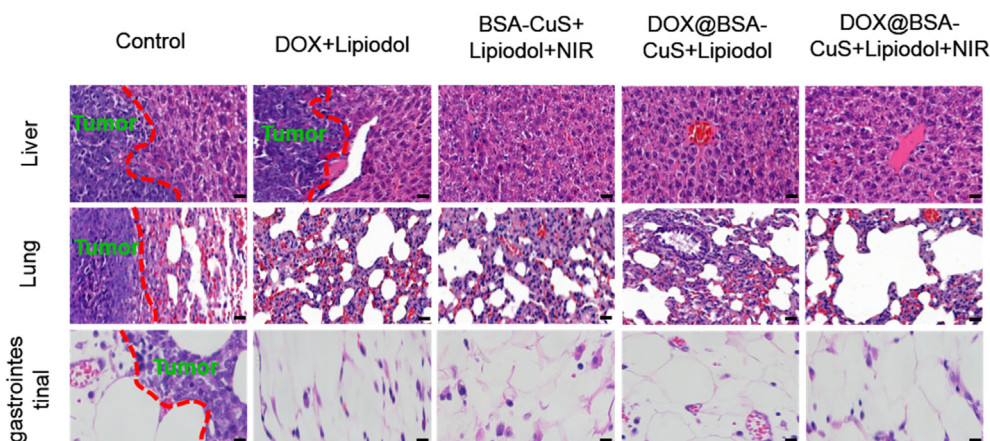
Fig. 8. Pathological examination of the therapeutic efficiency after different treatments at 10 days. Ten days after the operation, tumor metastasis occurred in the liver, lung, and gastrointestinal tract at the control group, and intrahepatic metastasis occurred in the DOX + Lipiodol group. Almost no tumor metastasis was found in the other three groups. Note: scale bar = 50 μm.

provided direct evidence that DOX was delivered and released through DOX@BSA-CuS *in vivo*.

The photothermal performance of DOX@BSA-CuS NPs *in vivo* was particularly investigated. In this study, the irradiance of 1.5 W/cm^2 was chosen for *in vivo* application to ensure that the threshold of photo-thermal ablation temperature was reached. In addition, the power density of 1.5 W/cm^2 for PTT has also been reported [42]. HCC tumor–bearing rats were administrated with DOX@BSA-CuS NP solution by the intra-arterial intervention method, and then, the tumor region was irradiated with NIR light. As exhibited in Fig. 5b and c, the temperature rose up to ~52 °C after 60 s of NIR irradiation and reached to ~62 °C at a time point of 300 s. In contrast, the temperature variation of the blank control group was less than 10 °C. These results demonstrate that the elevation of temperature is mainly dependent on BSA-CuS. Previous studies have reported that the cancer cells can be ablated above 42 °C [43]. One evident fact was that the temperature in the HCC area increased to 60 °C within 5 min after injection of CuS-BSA NPs combined with local NIR laser irradiation, whereas the temperature of the adjacent normal liver tissue did not increase significantly. This phenomenon is due to the distribution where CuS-BSA NPs are mainly concentrated in the tumor area after *trans*-hepatic injection. Therefore, the abovementioned results imply that BSA-CuS can effectively transform the NIR light into heat for PTT.

3.4. In vivo MRI-guided therapeutic efficacy of DOX@BSA-CuS NPs

The *in vivo* antitumor efficacy was further studied by measuring the tumor size estimated from MRI images and pathological examination (Fig. 6). The tumor volume is based on the calculation of maximum cross section. During the process of MRI examination, because of the multiple tests at different time points, the consistency of body position and liver location of SD rats in each test could not be fully achieved. Thus, all the tumors in MRI images cannot be unified in the same section. As revealed in Fig. 6a, real-time MRI images were utilized to monitor the tumor volume variation before and after the treatment. Tumors treated with DOX@BSA-CuS+Lipiodol with NIR irradiation exhibited the most significant tumor inhibition performance. Compared with the control group, tumor growth was obviously inhibited in the other four treatment groups at 3 d, 7 d, and 10 d. Particularly, DOX@BSA-CuS+Lipiodol combined with NIR irradiation achieved the most significant suppression effect (Fig. 6b). Meanwhile, the tumor weight at 10 days after treatment was measured, and the mean tumor weight in the DOX@BSA-CuS+Lipiodol with NIR irradiation–treated group was lightest, implying the best therapeutic effect (Fig. 6c). Subsequently, H&E staining results revealed that DOX@BSA-CuS+Lipiodol with NIR treatment exhibited the greater

suppression of tumor cell proliferation and enhancement of tumor cell necrosis than the other treatment groups (Fig. 6a).

Furthermore, the antitumor performance was also studied by immu-nohistochemical staining of the liver tumor tissues at 10 days after operation with different treatments. The results of TUNEL, Ki-67, and Caspase 3 demonstrated all treatment groups induced tumor cell necro-sis, apoptosis, and inhibition of proliferation compared with the control group (Fig. 7). Especially, DOX@BSA-CuS+Lipiodol+NIR treatment exhibited the most effective therapeutic performance. Meanwhile, the anti-angiogenic effect was further investigated by CD31 staining. Appreciable increase of CD31 expression was observed after emboliza-tion treatment groups, which may be due to the reason that the flow of blood to a tumor tissue could be blocked and subsequently to discernible tumor blood vessels [44]. However, CD31 expression displayed the lowest protein expression in the DOX@BSA-CuS+Lipiodol+NIR treat-ment group, indicating that the combination of photothermal treatment has a stronger tumor-killing ability. Meanwhile, the reduced tumor perfusion can decrease the heat dissipation and further promoted the PTT performance in the DOX@BSA-CuS+Lipiodol+NIR treatment group. In addition, H&E staining of the liver, lung, and gastrointestinal tract, where HCC easily metastasized, has demonstrated the rats in the control group developed liver, lung, and gastrointestinal metastasis, and intra-hepatic metastasis occurred in DOX+Lipiodol at 10 d after intervention (Fig. 8). On the contrary, almost no tumor metastasis was found in the other three groups. Therefore, DOX@BSA-CuS+Lipiodol+NIR treatment could effectively restrain the metastasis of live cancer cells.

3.5. In vivo preliminary assessment of the safety of DOX@BSA-CuS NPs

Hepatic toxicity and renal toxicity are common forms of toxicity during the course of TACE therapy for HCC and may reduce the effec-tiveness of TACE therapy or even cause death on their own [45]. Accordingly, assessing hepatic and renal toxicity after interventional therapy for HCC involving the transarterial introduction of DOX@BSA-CuS is an indispensable step for the clinical transformation application. MRI examination indicated that 3 days after DOX@BSA-CuS combined with NIR irradiation, high-signal peripheral edema appeared at the surface of the tumor tissue and in adjacent normal liver tissue (Fig. 6a). This phenomenon may be caused by the inflammation when the temperature of the surrounding tissue rises during the process of NIR irradiation. This peripheral edema began to disappear at a time point of 7d and completely disappeared by 10 d, suggesting that the combined therapy may cause mild transient damage to normal liver tissue. Simi-larly, the hepatorenal function–related blood biochemical indexes, including ALT, AST, CREA, and BUN, in the

DOX@BSA-CuS+Lipiodol+NIR treatment group were relatively increased after operation because of the effect of thermal ablation and efficient chemotherapy compared with other treatment groups. However, these indexes decreased gradually 1 day after operation, which was consistent with the regular treatment (DOX + Lipiodol). Meanwhile, hepatorenal function could nearly get back to the preoperative level after 7 days (Fig. S8). Overall, these phenomena were consistent with the changes in hepatorenal function when TACE was used clinically in conjunction with other local therapeutic methods, such as radio-frequency ablation and microwave ablation [46,47]. However, there were no postoperative deaths of rats induced by additional hepatorenal damage. Meanwhile, H&E staining results revealed that there were no pathological changes due to DOX@BSA-CuS NPs in the heart, liver without tumor, spleen, lung, and gastrointestinal tract at 10 days after operation with different treatments (Fig. S9). Therefore, the DOX@BSA-CuS NPs and the synergistic phototherapy exhibited relative safety.

4. Conclusion

In this work, the enhanced therapeutic effect against orthotopic HCC tumors was obtained by using the designed DOX@BSA-CuS nano-composite–mediated dual effects: hyperthermia and chemotherapy. The as-prepared BSA-CuS NPs exhibit stronger absorbance in the NIR region and photothermal effect to kill tumor cells, efficiently. Moreover, the external NIR laser–induced heating triggered the release of the DOX drug at the same time. The DOX@BSA-CuS and Lipiodol were injected by the intrahepatic arterial method for simultaneously delivering chemotherapy and phototherapy locally and ablated the orthotopic HCC tumors in the rat model. The *in vivo* results proved that the DOX@BSA-CuS and Lip-iodol with NIR irradiation exhibit the most remarkable necrosis of tumor and strongest antitumor effect, which can be monitored by MRI. Moreover, DOX@BSA-CuS+Lipiodol+NIR treatment can inhibit the liver tumor metastasis, efficiently. Finally, the preliminary safety evaluation demonstrates that direct arterial administration of the DOX@BSA-CuS during the therapeutic process has negligible toxicity on the rat. Therefore, our work provides a novel strategy for the construction of NIR-induced theranostic nanocomposites to be applied as potential intra-arterial embolic therapeutics for the treatment of orthotropic HCC.

Acknowledgements

Credit author statement

Fengyong Liu and Lifeng Liu guided all the experiments. Lifeng Liu, Xin Li and Hongjun Yuan prepared and completed the characterization analysis. Xin Li and Xiaomei Tian were responsible for biological examination. Xiaomei Tian and Jing Tang completed the pathological examination of the tissues, and the animal experiments were completed by Xin Li and Hongjun Yuan. Xin Li and Jing Tang performed all the cytology related experiments.

Declaration of competing interest

The authors declare that they have no known competing financial interests or personal relationships that could have appeared to influence the work reported in this paper.

Appendix A. Supplementary data

Supplementary data to this article can be found online at https://doi.org/10.1016/j.mtbio.2021.100128.

References

[1] J. He, D. Gu, X. Wu, K. Reynolds, X. Duan, C. Yao, J. Wang, C. Chen, J. Chen, R.P. Wildman, M.J. Klag, P.K. Whelton, Major causes of death among men and women in China, N. Engl. J. Med. 353 (2005) 1124–1134. https://doi:10.1056/nejmsa050467.

[2] A. Fujimoto, Y. Totoki, F. Hosoda, N.H. Hai, H. Nakagawa, Whole-genome sequencing analysis of 27 liver cancers, Genes Genet. Syst. 87 (2012) 402-402.

[3] R. Dutta, R.I. Mahato, Recent advances in hepatocellular carcinoma therapy, Pharmacol. Therapeut. (2017). https://doi:10.1016/j.pharmthera.2017.02.010.

[4] M. Schwartz, S. Roayaie, M. Konstadoulakis, Strategies for the management of hepatocellular carcinoma, Nat. Rev. Clin. Oncol. 4 (2007) 424–432. https://doi:10.1038/ncponc0844.

[5] C. Genco, G. Cabibbo, M. Maida, G. Brancatelli, M. Galia, N. Alessi, G. Butera, C. Genova, P. Romano, M. Raineri, Treatment of hepatocellular carcinoma: present and future, Expert Rev. Anticancer Ther. 13 (2013) 469–479. https://doi:10.1586/era.13.21.

[6] J. Llovet, T.B.X. For, L.C.G. Nic, Systematic review of randomized trials for unresectable hepatocellular carcinoma: chemoembolization improves survival, Hepatology 37 (2003) 429–442. https://doi:10.1053/jhep.2003.50047.

[7] S.Y. Lee, J.W. Choi, J. Lee, D. Kim, H. Kim, H. Cho, Hyaluronic acid/doxorubicin nanoassembly-releasing microspheres for the transarterial chemoembolization of a liver tumor, Drug Deliv. 25 (2018) 1472–1483. https://doi:10.1080/10717544.2018.1480673.

[8] A.L. Lewis, M.V. Gonzalez, A.W. Lloyd, B. Hall, Y. Tang, S.L. Willis, S.W. Leppard, L.C. Wolfenden, R.R. Palmer, P.W. Stratford, DC bead: in vitro characterization of a drug-delivery device for transarterial chemoembolization, J. Vasc. Intervent. Radiol. 17 (2006) 335–342. https://doi:10.1097/01.rvi.0000195323.46152.b3.

[9] M. Varela, M.I. Real, M. Burrel, A. Forner, M. Sala, M. Brunet, L. Ayuso, L. Castells, X. Montañá, J.M. Llovet, J. Bruix, Chemoembolization of hepatocellular carcinoma with drug eluting beads: efficacy and doxorubicin pharmacokinetics, J. Hepatol. 46 (2007) 474–481. https://doi:10.1016/j.jhep.2006.10.020.

[10] Q.F. Liu, Y.Y. Qian, P.L. Li, S.H. Zhang, J.J. Liu, X. Sun, M. Fulham, D. Feng, G. Huang, W. Lu, S. Song, ^{131}I-Labeled copper sulfide-loaded microspheres to treat hepatic tumors via hepatic artery embolization, Theranostics 8 (2018) 785–799. https://doi:10.7150/thno.21491.

[11] J. Zeng, L. Li, H. Zhang, J. Li, L. Liu, G. Zhou, Q. Du, C. Zheng, X. Yang, Radiopaque and uniform alginate microspheres loaded with tantalum nanoparticles for real-time imaging during transcatheter arterial embolization, Theranostics 8 (2018) 4591–4600. https://doi:10.7150/thno.27379.

[12] M.J. Song, H.J. Chun, D.S. Song, H.Y. Kim, S.H. Yoo, C. Park, S.H. Bae, J.Y. Choi, U.I. Chang, J.M. Yang, H.G. Lee, S.K. Yoon, Comparative study between doxorubicin-eluting beads and conventional transarterial chemoembolization for treatment of hepatocellular carcinoma, J. Hepatol. 57 (2012) 1244–1250. https://doi:10.1016/j.jhep.2012.07.017.

[13] R. Golfieri, E. Giampalma, M. Renzulli, R. Cioni, I. Bargellini, C. Bartolozzi, A.D. Breatta, G. Gandini, R. Nani, D. Gasparini, A. Cucchetti, L. Bolondi, F. Trevisani, B. O. T. P. On, I. S. G. PRECISION, Randomised controlled trial of doxorubicin-eluting beads vs conventional chemoembolisation for hepatocellular carcinoma, Br. J. Cancer 111 (2014) 255–264. https://doi:10.1038/bjc.2014.199.

[14] A.L. Lewis, M.R. Dreher, Locoregional drug delivery using image-guided intra-arterial drug eluting bead therapy, J. Contr. Release 161 (2012) 338–350. https://doi:10.1016/j.jconrel.2012.01.018.

[15] J. Zhao, W. Cui, Functional electrospun fibers for local therapy of cancer, Adv. Fiber Mater. 2 (2020) 229–245. https://doi:10.1007/s42765-020-00053-9.

[16] F. Deschamps, T. Isoardo, S. Denis, N. Tsapis, L. Tselikas, V. Nicolas, A. Paci, E. Fattal, T. de Baere, N. Huang, L. Moine, Biodegradable Pickering emulsions of Lipiodol for liver trans-arterial chemo-embolization, Acta Biomater. 87 (2019) 177–186. https://doi:10.1016/j.actbio.2019.01.054.

[17] L. Shen, Y.D. Zhang, J.L. Zhang, T. Wang, H.Y. Li, Y. Wang, D. Quan, Reversed lipid-based nanoparticles dispersed in iodized oil for transarterial chemoembolization, ACS Appl. Mater. Inter. 11 (2019) 20642–20648. https://doi:10.1021/acsami.9b03110.

[18] G. Li, Y. Chen, L. Zhang, M. Zhang, S. Li, L. Li, T. Wang, C. Wang, Facile approach to synthesize gold Nanorod@Polyacrylic acid/calcium phosphate yolk–shell nanoparticles for dual-mode imaging and pH/NIR-responsive drug delivery, Nano-Micro Lett. 10 (2017) 1–11. https://doi:10.1007/s40820-017-0155-3.

[19] R. Ge, X. Li, M. Lin, D.D. Wang, S.Y. Li, S.W. Liu, Q. Tang, Y. Liu, J. Jiang, L. Liu, H. Sun, H. Zhang, B. Yang, Fe₃O₄@polydopamine composite theranostic superparticles employing preassembled Fe₃O₄ nanoparticles as the core, ACS Appl. Mater. Inter. 8 (2016) 22942–22952. https://doi:10.1021/acsami.6b07997.

[20] P. Xue, R.H. Yang, L.H. Sun, Q. Li, L. Zhang, Z. Xu, Y. Kang, Indocyanine green-conjugated magnetic prussian blue nanoparticles for synchronous photothermal/photodynamic tumor therapy, Nano-Micro Lett. 10 (2018) 1–15. https://doi:10.1007/s40820-018-0227-z.

[21] Y.L. Liu, K.L. Ai, J.H. Liu, M. Deng, Y.Y. He, Dopamine-melanin colloidal nanospheres: an efficient near-infrared photothermal therapeutic agent for in vivo cancer therapy, Adv. Mater. 25 (2013) 1353–1359. https://doi:10.1002/adma.201204683.

[22] C. Zhang, Y.F. Yan, X.J. Zhang, C.S. Yu, Y. Zhao, K. Shao, S. Sun, BSA-directed synthesis of CuS nanoparticles as a biocompatible photothermal agent for tumor ablation in vivo, Dalton Trans. 44 (2015) 13112–13118. https://doi:10.1039/c5dt01467k.

[23] L. Liang, S.W. Peng, Z.W. Yuan, C. Wei, Y.Y. He, J. Zheng, Y. Gu, H. Chen, Biocompatible tumor-targeting nanocomposites based on CuS for tumor imaging

and photothermal therapy, RSC Adv. 8 (2018) 6013–6026. https://doi:10.1039/c7ra12796k.

[24] X.J. Su, F.F. Zhao, Y.H. Wang, X.S. Yan, S.N. Jia, B. Du, CuS as a gatekeeper of mesoporous upconversion nanoparticles-based drug controlled release system for tumor-targeted multimodal imaging and synergetic chemo-thermotherapy, Nanomed-Nanotechnol. 13 (2017) 1761–1772. https://doi:10.1016/j.nano.2017.03.008.

[25] H. Shi, Y. Sun, R. Yan, S. Liu, L. Zhu, S. Liu, Y. Feng, P. Wang, J. He, Z. Zhou, Magnetic semiconductor Gd-doping CuS nanoparticles as activatable nanoprobes for bimodal imaging and targeted photothermal therapy of gastric tumors, Nano Lett. 19 (2019) 937–947. https://doi:10.1021/acs.nanolett.8b04179.

[26] Z. Ouyang, D. Li, Z. Xiong, C. Song, Y. Gao, R. Liu, M. Shen, X. Shi, Antifouling dendrimer-entrapped copper sulfide nanoparticles enable photoacoustic imaging-guided targeted combination therapy of tumors and tumor metastasis, ACS Appl. Mater. Interfaces 13 (2021) 6069–6080. https://doi:10.1021/acsami.0c21620.

[27] A. Curcio, A.V. de Walle, E. Benassai, A. Serrano, N. Luciani, N. Menguy, B.B. Manshian, A. Sargsian, S. Soenen, A. Espinosa, A. Abou-Hassan, C. Wilhelm, Massive intracellular remodeling of CuS nanomaterials produces nontoxic bioengineered structures with preserved photothermal potential, ACS Nano 15 (2021) 9782–9795. https://doi:10.1021/acsnano.1c00567.

[28] W.W. Mu, Q.H. Chu, Y.J. Liu, N. Zhang, A review on nano-based drug delivery system for cancer chemoimmunotherapy, Nano-Micro Lett. 12 (2020). https://doi:10.1007/s40820-020-00482-6.

[29] K. Yang, G.B. Yang, L. Chen, L. Cheng, L. Wang, C. Ge, Z. Liu, FeS nanoplates as a multifunctional nano-theranostic for magnetic resonance imaging guided photothermal therapy, Biomaterials 38 (2015) 1–9. https://doi:10.1016/j.biomaterials.2014.10.052.

[30] J. Wang, L. Fang, P. Li, L. Ma, W.D. Na, C. Cheng, Y. Gu, D. Deng, Inorganic nanozyme with combined self - oxygenation/degradable capabilities for sensitized cancer immunochemotherapy, Nano-Micro Lett. 11 (2019) 1–18. https://doi:10.1007/s40820.

[31] S. Wilhelm, A.J. Tavares, Q. Dai, S. Ohta, J. Audet, H.F. Dvorak, W.C.W. Chan, Analysis of nanoparticle delivery to tumors, Nat. Rev. Mater. 1 (2016). https://doi:10.1038/natrevmats.2016.14.

[32] C. Chen, Z. Wu, P. Ding, N. Sun, R. Pei, Peptide NGR modified TiO₂ nanofiber substrate for circulating tumor cells capture, Adv. Fiber Mater. 2 (2020) 186–193. https://doi:10.1007/s42765-020-00040-0.

[33] M.M. Rashed, N.H.A. Al-Mudallal, A.A. Taha, Reduce the toxicity of prepared copper sulfide nanoparticles, J. Pharmacol. Sci. 10 (2019). https://doi:10.26452/ijrps.v10i3.1433.

[34] M. Mahanthappa, S. Yellappa, N. Kottam, C.S.R. Vusa, Sensitive determination of caffeine by copper sulphide nanoparticles modified carbon paste electrode, Sensor Actuat A.-Phys. 248 (2016) 104–113. https://doi:10.1016/j.sna.2016.07.013.

[35] Z.Q. Xu, S.C. Wu, G.C. Huang, H.W. Ding, R.J. Gui, B.H. Zhu, Aptamer-modified CuS nanocrystals/graphene oxide composites for controlled release of glucosamine and chemo-photothermal therapy of tumor cells, Mater. Lett. 195 (2017) 131–135. https://doi:10.1016/j.matlet.2017.02.119.

[36] W. Wang, X. Cheng, J. Liao, Z. Lin, L. Chen, D. Liu, T. Zhang, L. Li, Y. Lu, H. Xia, Synergistic photothermal and photodynamic therapy for effective implant-related bacterial infection elimination and biofilm disruption using Cu9S8 nanoparticles, ACS Biomater. Sci. Eng. 5 (2019) 6243–6253. https://doi:10.1021/acsbiomaterials.9b01280.

[37] D.K. Roper, W. Ahn, M. Hoepfner, Microscale heat transfer transduced by surface plasmon resonant gold nanoparticles, J. Phys. Chem. C Nanomater. Interfaces 111 (2007) 3636–3641. https://doi:10.1021/jp064341w.

[38] L. Zhu, D. Gao, L. Xie, Y. Dai, Q. Zhao, NIR II-excited and pH-responsive ultrasmall nanoplatform for deep optical tissue and drug delivery penetration and effective cancer chemophototherapy, Mol. Pharm. 17 (2020). https://doi:10.1021/acs.molpharmaceut.0c00404.

[39] Y.Y. Li, Y.R. Zhou, T.X. Gu, G. Wang, Z.H. Ren, W. Weng, X. Li, G. Han, C. Mao, A multifunctional nanocrystalline CaF2: Tm, Yb@mSiO2 system for dual-triggered and optically monitored doxorubicin delivery, Part. Part. Syst. Char. 33 (2016) 896–905. https://doi:10.1002/ppsc.201600166.

[40] J.B. W, Y.L. C, M.W. G, Local drug delivery strategies for cancer treatment: gels, nanoparticles, polymeric films, rods, and wafers, J. Contr. Release 159 (2012) 14–26. https://doi:10.1016/j.jconrel.2011.11.031.

[41] M. Tian, W. Lu, R. Zhang, C. Xiong, J. Ensor, J. Nazario, J. Jackson, C. Shaw, K.A. Dixon, J. Miller, Tumor uptake of hollow gold nanospheres after intravenous and intra-arterial injection: PET/CT study in a rabbit VX2 liver cancer model, Mol. Imag. Biol. 15 (2013) 614–624. https://doi:10.1007/s11307-013-0635-x.

[42] R.A. Sheth, X. Wen, J. Li, M.P. Melancon, S. Gupta, Doxorubicin-loaded hollow gold nanospheres for dual photothermal ablation and chemoembolization therapy, Cancer Nanotechnol. 11 (2020) 1–16. https://doi:10.1186/s12645-020-00062-8.

[43] R. Mrówczyński, Polydopamine-based multifunctional (nano) materials for cancer therapy, ACS Appl. Mater. Inter. 10 (2018) 7541–7561. https://doi:10.1021/acsami.7b08392.

[44] Z. von Marschal, T. Cramer, M. Höcker, G. Finkenzeller, B. Wiedenmann, S. Rosewicz, Dual mechanism of vascular endothelial growth factor upregulation by hypoxia in human hepatocellular carcinoma, Gut 48 (2001) 87–96. https://doi:10.1136/gut.48.1.87.

[45] R. Lencioni, T.D. Baere, M.C. Soulen, W.S. Rilling, J.F.H. Geschwind, Lipiodol transarterial chemoembolization for hepatocellular carcinoma: a systematic review of efficacy and safety data, Hepatology 64 (2016) 106–116. https://doi:10.1002/hep.28453.

[46] Z.J. Wang, M.Q. Wang, F. Duan, P. Song, F.Y. Liu, Z.F. Chang, Y. Wang, J.Y. Yan, K. Li, Transcatheter arterial chemoembolization followed by immediate radiofrequency ablation for large solitary hepatocellular carcinomas, World J. Gastroenterol. 19 (2013) 4192–4199. https://doi:10.3748/wjg.v19.i26.4192.

[47] Z.N. Li, D.C. Jiao, X.W. Han, G.Y. Si, Y.H. Li, J.F. Liu, Y. Xu, B. Zheng, X. Zhang, Transcatheter arterial chemoembolization combined with simultaneous DynaCT-guided microwave ablation in the treatment of small hepatocellular carcinoma, Canc. Imag. 20 (2020) 13–19. https://doi:10.1186/s40644-020-0294-5.